Chapter 10
Half-Heusler Thermoelectrics

Ran He, Hangtian Zhu, and Shuo Chen

Abstract Half-Heusler (HH) compounds are superb thermoelectric (TE) materials due to combined features of excellent TE performances, high thermal stability, mechanical robustness, simple contact, and non-toxicity. Over the past two decades, significant improvements in TE properties have been realized in a variety of compounds. Here we summarize the recent development of TE properties of HH compounds with special emphasis on the experimentally demonstrated strategies such as alloying effects, energy filter effects, nanostructuring, band convergence, etc. that were beneficial to improve TE performances.

10.1 Introduction

Burning nonrenewable fossil fuels satisfies ~80% of global energy consumptions. In this process, however, over 50% of produced energy is not used for its intended purpose and rejected as waste heat. Techniques that are capable of recovering even a small portion of waste heat could generate great benefits economically and environmentally. Thermoelectric generators (TEGs) operating on the basis of thermoelectric effects can convert some of waste heat into electricity, improve the efficiency, and reduce consumption of fossil fuel. TEGs are special due to solid-state nature. TEGs are reliable, noiseless, scalable, and maintenance free. The drawback of TEG is relatively low efficiency due to limited performance of TE materials and high cost of generated power. Therefore, it is crucially important to boost TE performances of TE materials and/or to reduce significantly those costs.

For ideal TEG, where heat can be supplied and removed effectively, and with negligible contact losses, heat-to-power conversion efficiency (η) can be expressed as:

R. He (✉)
Leibniz Institut für Festkörper- und Werkstoffforschung Dresden e.V., Institut für Metallische Werkstoffe, Dresden, Germany
e-mail: r.he@ifw-dresden.de

H. Zhu · S. Chen
Department of Physics and TcSUH, University of Houston, Houston, TX, USA

S. Skipidarov, M. Nikitin (eds.), *Novel Thermoelectric Materials and Device Design Concepts*, https://doi.org/10.1007/978-3-030-12057-3_10

$$\eta = \frac{T_h - T_c}{T_h} \times \frac{\sqrt{1 + ZT_{avg}} - 1}{\sqrt{1 + ZT_{avg}} + \frac{T_c}{T_h}}, \tag{10.1}$$

where T_h and T_c are temperatures on hot and cold side and ZT_{avg} is average value of TE figure-of-merit ZT of TE material in temperature gradient between T_c and T_h.

$$ZT = \frac{PF}{\kappa} T, \tag{10.2}$$

$$PF = \frac{S^2}{\rho} = S^2 \sigma, \tag{10.3}$$

$$\kappa = \kappa_e + \kappa_L, \tag{10.4}$$

where PF, T, κ, S, ρ, σ, κ_e, and κ_L are power factor, absolute temperature, total thermal conductivity, Seebeck coefficient, electrical resistivity, electrical conductivity, electronic thermal conductivity, and lattice thermal conductivity, respectively. Consequently, higher ZT corresponds to higher conversion efficiency.

Among various TE materials, HH compounds are one of the most promising candidates for heat-to-power energy conversion applications. HH compounds are crystallized in the space group $F\bar{4}3m$ with three interpenetrating face-centered cubic (fcc) structures. HH compounds possess the general formula *XYZ*, where *X*, *Y*, and *Z* occupy Wyckoff positions $4b(\frac{1}{2}, \frac{1}{2}, \frac{1}{2})$, $4c(\frac{1}{4}, \frac{1}{4}, \frac{1}{4})$ and $4a(0, 0, 0)$, respectively, and $4d(\frac{3}{4}, \frac{3}{4}, \frac{3}{4})$ positions are voids. Among hundreds of HH compounds, HHs with valence electron count 8 and 18 are potential TE materials due to semiconductors' nature [1]. The robustness of HH compounds originates from the properties of decent figure-of-merit, ZT [2–12], high mechanical and thermal stability [5, 13, 14], low cost [15], low toxicity, and ultrahigh output power density [16, 17]. The only drawback of HHs is relativity high κ, especially κ_L. Therefore, suppressing the phonon transport is crucial for obtaining high performance TE properties in HH compounds.

Among the various HH compounds, *M*NiSn- and *M*CoSb-based compounds (M = Hf, Zr, Ti) are the most widely studied *n*- and *p*-type HH materials. In recent years, TE properties of *n*-type *M*CoSb and *p*-type NbFeSb- and ZrCoBi-based compounds were also investigated, and promising ZT have been reported [6, 18–20]. For example, Fu et al. reported high ZT reaching 1.47 in Hf-doped NbFeSb at 1200 K [17]. Zhu et al. realized similar ZT ~ 1.42 in ZrCoBi-based compounds at lower temperature (973 K) [20]. He et al. reported a record high PF ~ 106 $\mu W \times cm^{-1} \times K^{-2}$ in Ti-doped NbFeSb at room temperature, which, subsequently, yielded a record output power density of ~22 $W \times cm^{-2}$ in between 293 K and 868 K [16]. These works boost greatly the applicability of HH compounds for TE power generation.

Successful improvement of TE properties in half-Heusler compounds was realized through either reducing in κ or boosting PF. For reducing κ, approaches such as nanoparticle inclusion, bulk nanostructuring, phase separations, alloying effects, etc.

have been studied, while strategies such as band engineering, tuning the scattering mechanism, and energy filter effects, etc. have been introduced for increasing in PF. In this chapter, we introduce these strategies in detail and present those effects in improving TE performances of HH compounds.

10.2 Suppressing the Thermal Conductivity

10.2.1 Suppressing Thermal Conductivity in Single Phase

Because of the small phonon group velocity of the optic branch, most of the heat transport in the material is attributed to acoustic branch [21]. Therefore, κ_L can be described by Callaway model [22]:

$$\kappa_L = \frac{1}{3}\int_0^{\omega_{max}} C_s(\omega)\nu_g(\omega)^2\tau(\omega)d\omega, \tag{10.5}$$

where ω is frequency of phonon, C_s is spectral heat capacity, v_g is phonon group velocity, and τ is phonon relaxation time. Assuming that phonon distribution follows Boltzmann equation [21], Eq. (10.5) can be rewritten as:

$$\kappa_L = \frac{k_B}{2\pi^2\nu_{ph}}\left(\frac{k_B T}{\hbar}\right)^3\int_0^{\theta_D/T}\frac{x^4 e^x}{\tau_C^{-1}(e^x-1)^2}dx, \tag{10.6}$$

where k_B is Boltzmann constant, v_{ph} is phonon velocity, $\hbar$ is reduced Planck constant, θ_D is Debye temperature, τ_C is combined (total) phonon relaxation time, and $x = \frac{\hbar\omega}{k_B T}$ is dimensionless variable for integration. Based on this equation, κ_L can be regarded as function of v_{ph}, θ_D, and total relaxation time τ_C. Total relaxation time τ_C is determined by combined effect of various phonon scattering processes. Assuming all scattering process is independent to each other, ${\tau_C}^{-1}$ can be estimated as the sum of reciprocals of relaxation times for different processes:

$$\tau_C^{-1} = \sum_i \tau_i^{-1} \tag{10.7}$$

Low κ of TE material is one of essential requirements for achieving high thermoelectric performance. Seeking new materials with intrinsically low κ_L and developing effective strategies to suppress κ of state-of-the-art TE materials become two most important approaches to improve ZT value.

The Strategies to Suppress Thermal Conductivity

Umklapp process, which is determined by intrinsic properties of the material, is the key process for phonon scattering in single crystal and dominates in high temperature thermal transport in all materials. In comparison to most of promising TE materials that have intrinsically low κ_L, half-Heusler compounds possess relatively high κ_L due to the strong bonding that facilitate phonon transport. Seeking HH compounds with intrinsically low κ_L is a good starting point on which further reduction can be achieved through manipulating the microstructure. Therefore, understanding the origins of low κ_L is beneficial to identify new promising TE materials.

Usually κ_L can be expressed as [21, 23]:

$$\kappa_L = \frac{1}{3} c_v v_{ph} l, \tag{10.8}$$

where c_v is specific heat and v_{ph} is phonon velocity, while l is phonon mean free path. In single crystal, especially, at temperature much higher than θ_D, Umklapp scattering is dominant in phonon propagation. As will be shown later, extensive works have been introduced to reduce phonon mean free path. Meanwhile, v_{ph} as another important parameter determining κ_L can also be tailored for phonon engineering. Usually, v_{ph} is simply approximated by low-frequency sound velocity $v \propto \sqrt{\frac{B}{\delta}}$, where B is elastic modulus and δ is density of compound. Therefore, materials with low v usually tend to have low κ_L.

This was demonstrated in a comparative study of TiCoSb-, ZrCoSb-, and ZrCoBi-based HH compounds [20]. Figure 10.1 shows relationship between mean sound velocity v_m and Young's modulus E of several HH compounds. In comparison to Sn- and Sb-based half-Heusler compounds, ZrCoBi possesses the

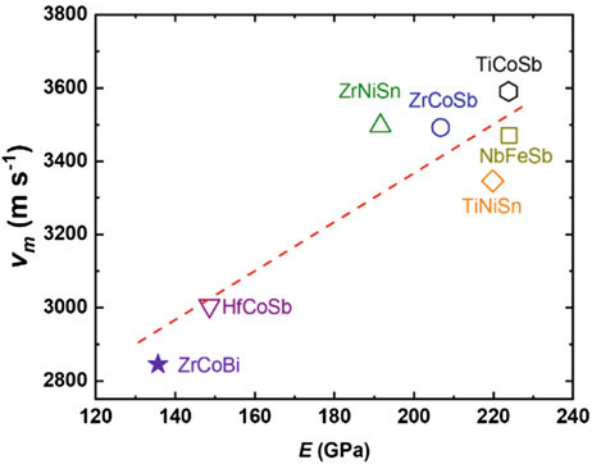

Fig. 10.1 Relationship between Young's modulus E and mean sound velocity v_m of several HH compounds [20]

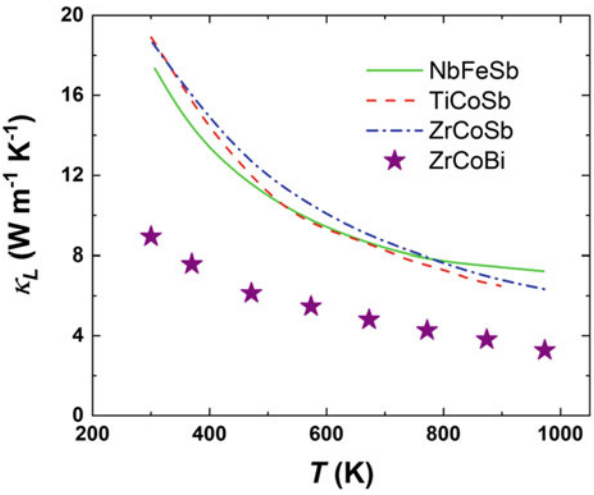

Fig. 10.2 Temperature-dependent κ_L of undoped NbFeSb, TiCoSb, ZrCoSb, and ZrCoBi [20]

lowest $v_m \sim 2850\ m \times s^{-1}$ and Young's modulus. Low v and E originate from weaker chemical bonding and heavy atomic mass of Bi. For ZrCoBi-based compounds, strong relativistic effect of Bi contracts 6*s* shell and increases in its inertness for bonding. Therefore, low v_m and E will jointly contribute to intrinsically low κ_L of ZrCoBi.

Temperature-dependent thermal conductivities of several undoped HH compounds are plotted in Fig. 10.2 including NbFeSb, TiCoSb, ZrCoSb, and ZrCoBi [16, 19, 20, 24]. The pristine ZrCoBi shows much lower κ_L compared to the other HHs. Room temperature κ_L is equal to $\sim 19\ W \times m^{-1} \times K^{-1}$ for TiCoSb, $\sim 19\ W \times m^{-1} \times K^{-1}$ for ZrCoSb, and $\sim 17\ W \times m^{-1} \times K^{-1}$ for NbFeSb, but $\sim 9\ W \times m^{-1} \times K^{-1}$ for ZrCoBi, which is only half of the other *p*-type HHs. Significant suppressing of κ_L originates from reduced v_{ph} and low E, as suggested in Fig. 10.1 and Eq. (10.8). Based on intrinsic low κ_L, subsequent strategies were employed to further suppress κ_L, such as alloying effects and nano-bulk structuring. As a result, low $\kappa_L \sim 2.2\ W \times m^{-1} \times K^{-1}$ were realized in ZrCoBi-based compounds which further yields high ZT ~ 1.42 at 973 K, which is one of the highest value at this temperature among HH compounds [20].

However, Umklapp process is not the only source in single-phase material for phonon scattering. In real TE material, phonon has to pass through specific microstructure to transport heat and may be scattered by all kind of boundaries, point defects, dislocations, etc., that are strongly related to material processing and synthesis. Therefore, thermal conductivity reduction is the result of various scattering processes, mostly from grain boundary scattering and point defect scattering for HH compounds.

Nano-bulk structuring. Polycrystalline materials are composed of many grains with varying size and orientation. In recent years, the technique to controlling size and arrangement of the grain has been applied in TE material to manipulate of transport properties. Grain boundary can provide very effective low-frequency

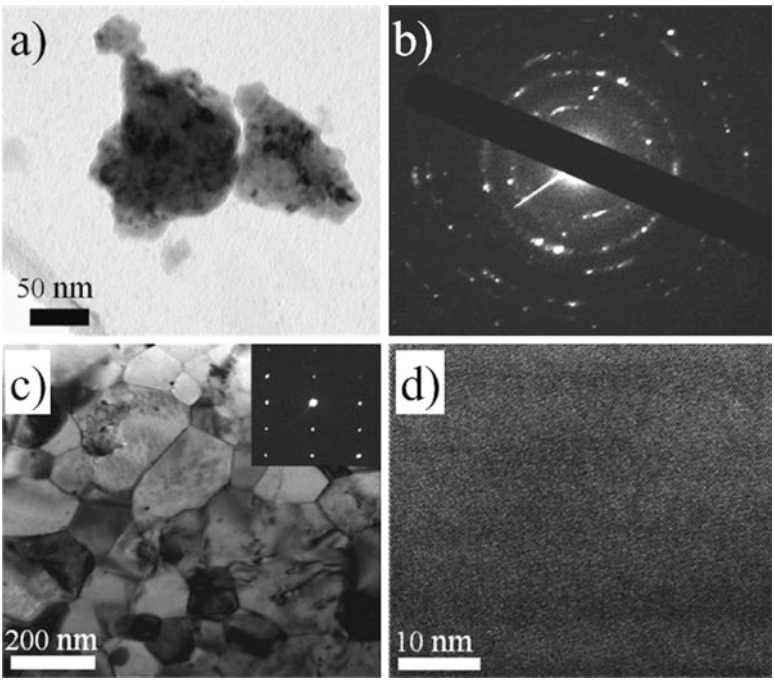

Fig. 10.3 Transmission electron microscopy (TEM) characterizations of nanostructured HH. (**a**) TEM image of the powders of $Hf_{0.5}Zr_{0.5}CoSb_{0.8}Sn_{0.2}$ after ball milling. (**b**) Electron diffraction pattern of selected area showing the polycrystalline nature of agglomerated cluster in **a**). (**c**) Low magnification TEM image of hot-pressed $Hf_{0.5}Zr_{0.5}CoSb_{0.8}Sn_{0.2}$, showing grain size of ~200 nm. Inset: Selected area electron diffraction (SAED) pattern of one grain showing single crystallization. (**d**) High-resolution TEM image showing crystallinity at atomic level [2]

phonon scattering $\tau_B^{-1} \sim \omega^0$ at low temperature. A significant performance improvement has been demonstrated in bulk $Hf_{0.5}Zr_{0.5}CoSb_{0.8}Sn_{0.2}$ with nano-bulk structuring [2]. Nanocrystalline bulk material is prepared by ball milling of arc-melted ingot to obtain nanopowders, which were sintered into a dense sample using spark plasma sintering (SPS) or hot pressing at elevated temperatures (from ~1100 to 1150 °C) and external pressure (from 50 MPa to 80 MPa). Figure 10.3a, b shows that grain sizes after ball milling are usually of ~10 nm; meanwhile, SPS samples are well crystallized with average grain size of ~200 nm, as shown in Fig. 10.3c, d. The obtained grain size is much smaller comparing with the samples prepared by using other approaches, where grain sizes are usually in the order of 10–100 μm.

Figure 10.4 shows compared TE properties of bulk and nanostructured $Hf_{0.5}Zr_{0.5}CoSb_{0.8}Sn_{0.2}$. Nanostructured compounds possess higher S and lower σ, as shown in Fig. 10.4a, b. PF of nanostructured compounds are slightly higher than bulk counterpart, as shown in Fig. 10.4c. On the other hand, a significant drop of κ occurs in nanostructured sample, as shown in Fig. 10.4d. Figure 10.4e shows similar

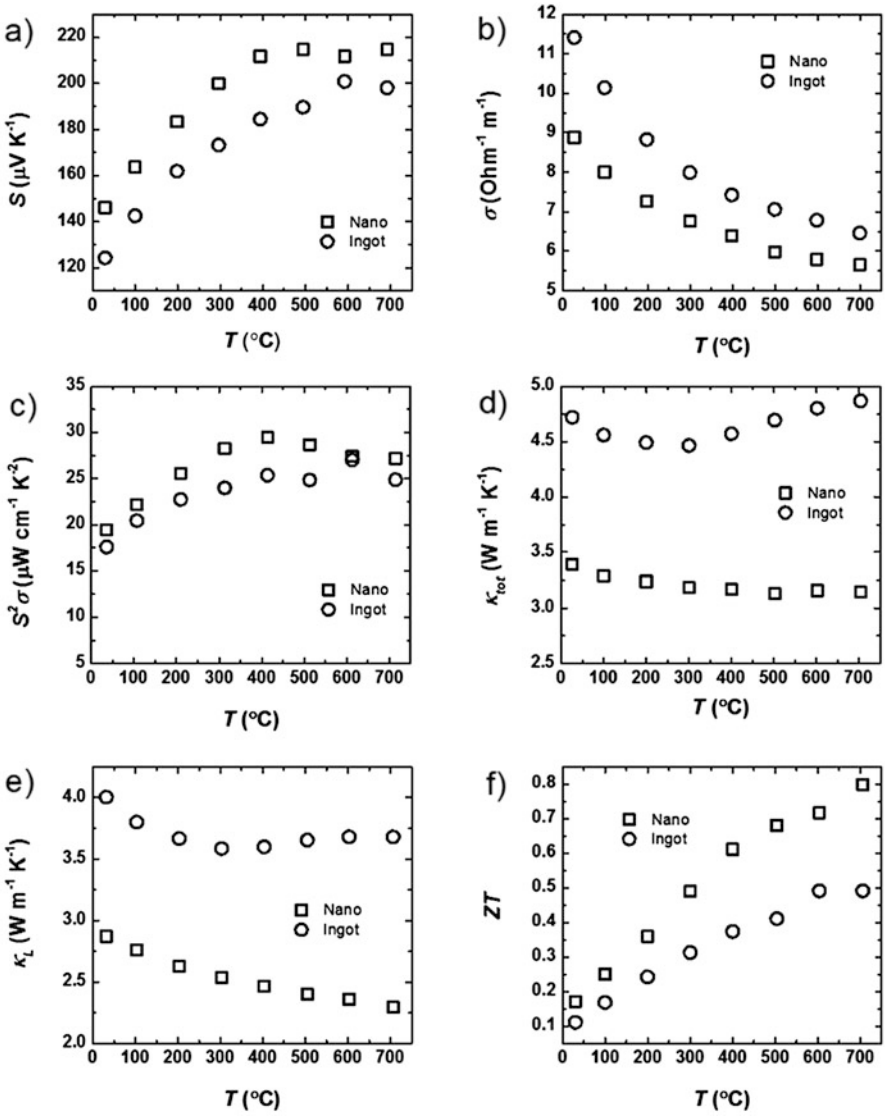

Fig. 10.4 Temperature-dependent (**a**) S, (**b**) σ, (**c**) PF, (**d**) κ, (**e**) κ_L, and (**f**) ZT of ball milled and hot-pressed $Hf_{0.5}Zr_{0.5}CoSb_{0.8}Sn_{0.2}$ sample in comparison with that of the ingot [2]

decreasing in κ_L. As a result, peak ZT ~ 0.8 has been achieved. In comparison, bulk ingot possesses of peak ZT ~ 0.5 with identical nominal compositions. Ball milling and hot-pressing techniques have also been proved very effective in preparing HH compounds with different composition, and remarkable improvements have been demonstrated [2, 4].

Point defect scattering. Fluctuations of mass and strain in the atomic scale have been employed to scatter phonon effectively. The intrinsic nature of ternary HH compounds provides great opportunity to introduce point defects. Specifically, partial substitution of isoelectric element is widely studied due to its minimum effects on transport of charge carriers. For example, *M* site in *M*CoSb- and *M*NiSn-based compounds could be arbitrary combinations of Hf, Zr, and Ti, albeit phase separations might occur. Due to κ sensitivity to composition ZT, optimization is possible. As an example, Fig. 10.5 shows TE properties of compounds $Hf_{1-x}Zr_xCoSb_{0.8}Sn_{0.2}$ and $Hf_{1-y}Ti_yCoSb_{0.8}Sn_{0.2}$ with diatomic and $Hf_{1-x-y}Zr_xTi_yCoSb_{0.8}Sn_{0.2}$ with triatomic combination on *M* site [2–4, 15]. Specifically noted from Fig. 10.5e, $Hf_{1-y}Ti_yCoSb_{0.8}Sn_{0.2}$ with diatomic combination on *M* site possesses much lower κ than the other two groups of compounds (diatomic $Hf_{1-x}Zr_xCoSb0.8Sn0.2$ and triatomic $Hf_{1-x-y}Zr_xTi_yCoSb_{0.8}Sn_{0.2}$) as a result of stronger point defect scattering because of larger difference between atomic mass Hf/Ti. The variation trends of κ show the effects of point defect scattering in TE performances of HH compounds.

10.2.2 Thermal Conductivity Suppression with Mixed Phases

Nanoinclusions

The reduction in κ could also be realized through a mixture of multiple phases. The lattice mismatch across phase boundaries serves as scattering center in phonon propagation. Note that the inclusion of secondary phases also scatters charge carrier, therefore, this approach is particularly useful for compounds with high κ, such as HHs, where the phonon transport could be more sensitive than electron transport to presence of secondary phases. Besides, tunable parameters, such as size and Fermi level of the inclusion, can be employed to filter low-energy electrons and thus benefits *S*. Experimentally, such effects were realized in HH compounds either through introduction of secondary phases, such as oxides or with phase decompositions from nominal compositions, such as phase separation and half-Heusler/full-Heusler (HH/FH) mixtures.

It's straightforward to decrease κ by incorporating dispersed secondary phases as phonon scattering centers. Experimentally reported are oxides include Al_2O_3, C_{60}, WO_3, NiO, and MO_2 in *M*CoSb- and *M*NiSn-based compounds with *M* being Hf, Zr, or Ti [25–31]. These oxides could be introduced either in situ or ex situ. Hsu et al. studied the effects of HfO_2 inclusions in TE properties of $Zr_{0.5}Hf_{0.5}CoSb_{1-x}Sn_x$ [32]. The in situ grown HfO_2 powders were obtained through ball milling of arc-melted ingots under atmosphere pressure (1 atm, 25 °C and 40% RH). Obtained powders were sintered at 1373 K for 15 mins under 80 MPa by SPS process. The dispersed HfO_2 nanoparticles at interfaces between grains not only impede phonon transport, but also impede grain growth during SPS procedure, which could further enhance phonon scattering. κ of HH compounds with dispersed HfO_2 was suppressed greatly. Peak ZT ~ 0.8 was obtained at 873 K, which is similar to nano-bulk structured HH compounds.

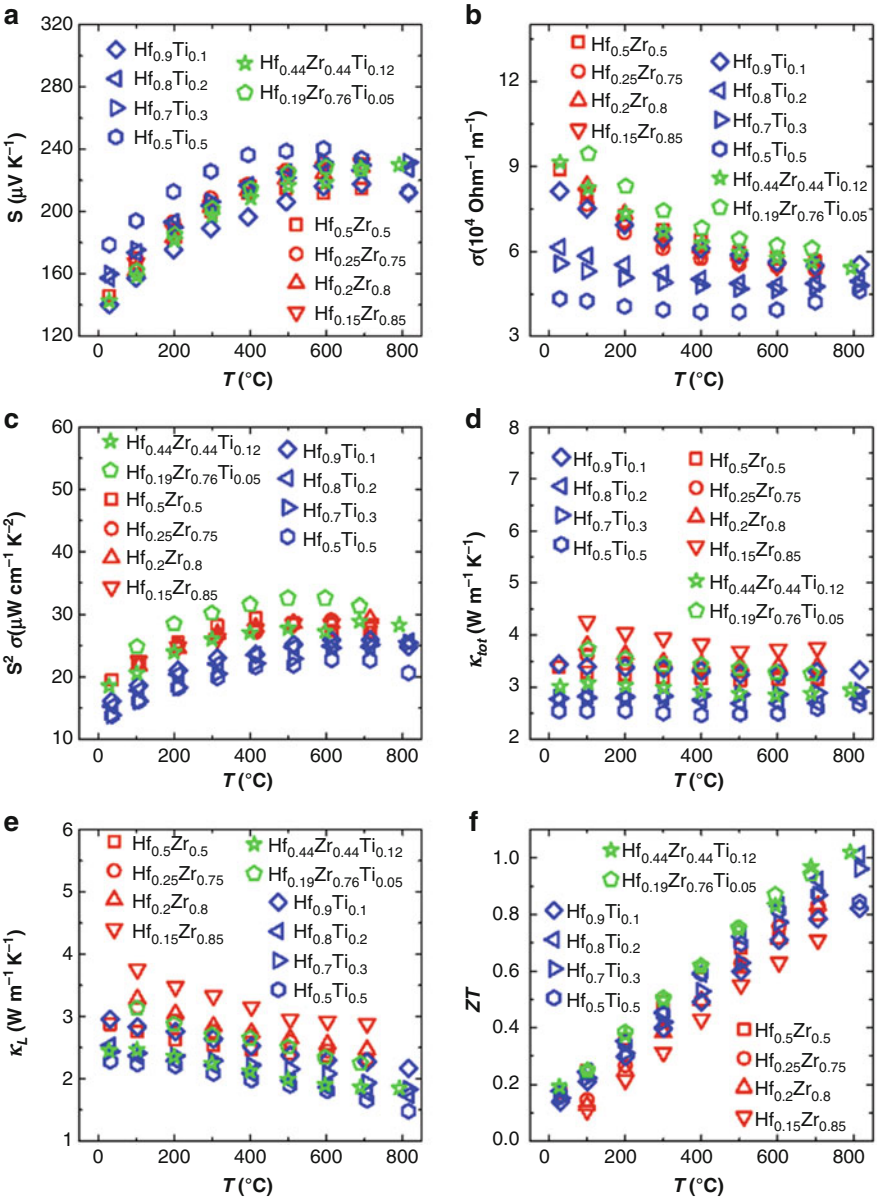

Fig. 10.5 Temperature-dependent (**a**) S, (**b**) σ, (**c**) PF, (**d**) κ, (**e**) κ_L, and (**f**) ZT of nanostructured $M\text{CoSb}_{0.8}\text{Sn}_{0.2}$

In another work by Poon et al., approximately 1–2 vol. % of ZrO_2 nanoparticles were mixed with $Hf_{0.3}Zr_{0.7}CoSn_{0.3}Sb_{0.7}$ powders [31]. TEM observation suggests ZrO_2 particles with grain size from ~50 to 80 nm at interfaces between grains, while

typical grain sizes of main matrix are 5–25 μm. TE properties of *p*-type $Hf_{0.3}Zr_{0.7}CoSn_{0.3}Sb_{0.7}$ with and without 2 vol. % ZrO_2 nanoparticles additive were comparatively plotted in Fig. 10.6. Figure 10.6a shows that ρ increases upon addition of ZrO_2 since it is an insulator. Second-phase nanoparticles can also serve as potential barriers that prohibit low-energy charge carriers from passing through the grain boundaries, hence increasing S (Fig. 10.6b). Similar effects were also reported in HH compounds with InSb semiconductor nanoparticles [33]. Overall PF increases by up to ~13% at 970 K, as shown in Fig. 10.6c. On the other hand, κ is suppressed, especially, at elevated temperatures (Fig. 10.6d). Increased PF and suppressed κ yield increase in ZT of ~23% from 0.65 to 0.8 at 970 K (Fig. 10.6e).

Another type of inclusions, such as InSb compound and FH alloys, could not only enhance phonon scattering but also benefit charge carriers transport due to energy filter effect at the boundaries. Xie et al. studied TE properties of $TiCo_{0.85}Fe_{0.15}Sb$ with x at. % in situ formed InSb [34]. All TE parameters were simultaneously enhanced with up to 1.0 at. % InSb, i.e., σ and S become higher, and κ_L becomes lower. As shown in Fig. 10.7a, b, improved σ is due to enhanced mobility of charge carriers since mobility in TiCoSb is as low as ~0.5 $cm^2/(V \times s)$, while InSb has very high mobility of charge carriers on the order of ~10^4 $cm^2/(V \times s)$ for electrons and ~10^3 $cm^2/(V \times s)$ for holes. Furthermore, the presence of InSb yields energy filter effects, as suggested by decreased concentration of charge carriers (Fig. 10.7b) and increased S (Fig. 10.7c). Therefore, PF is greatly improved with up to 1 at. % InSb inclusions (Fig. 10.7d).

On the other hand, κ shows also descending trend with respect to increased InSb content up to 1.5 at. %, as shown in Fig. 10.7e; κ decreases not only because InSb is secondary phase but also because precipitated InSb on the grain boundaries impedes the growth of grains, which yields a stronger phonon scattering.

Figure 10.7f shows peak ZT ~ 0.3 at ~ 925 K with 1 at. % InSb inclusions as a result of simultaneously improvement of all three TE parameters. Note that with content of InSb inclusions more than 1.0 at. %, TE properties become worse, showing the existence of optimum InSb concentration. As seen from Fig. 10.7b, with InSb content exceeding 1.5 at. %, mobility of charge carriers dropped, and concentration increased. This suggests the disappearing of energy filtering effect. Similar effects were also observed in half-Heusler compounds with FH inclusions [35–37].

A small concentration of FH precipitations could effectively enhance S and σ and suppress κ [37]. In both cases, of InSb or FH inclusions, the energy filter effect originates from enlarged band gap due to the quantum confinement effects. Therefore, precipitates should be small enough; otherwise the energy filter effect vanishes. This is, indeed, the case, since there exists a maximum concentration of these precipitates, beyond which TE properties decays greatly. The details of energy filter effects will be discussed in Sect. 10.3.3.

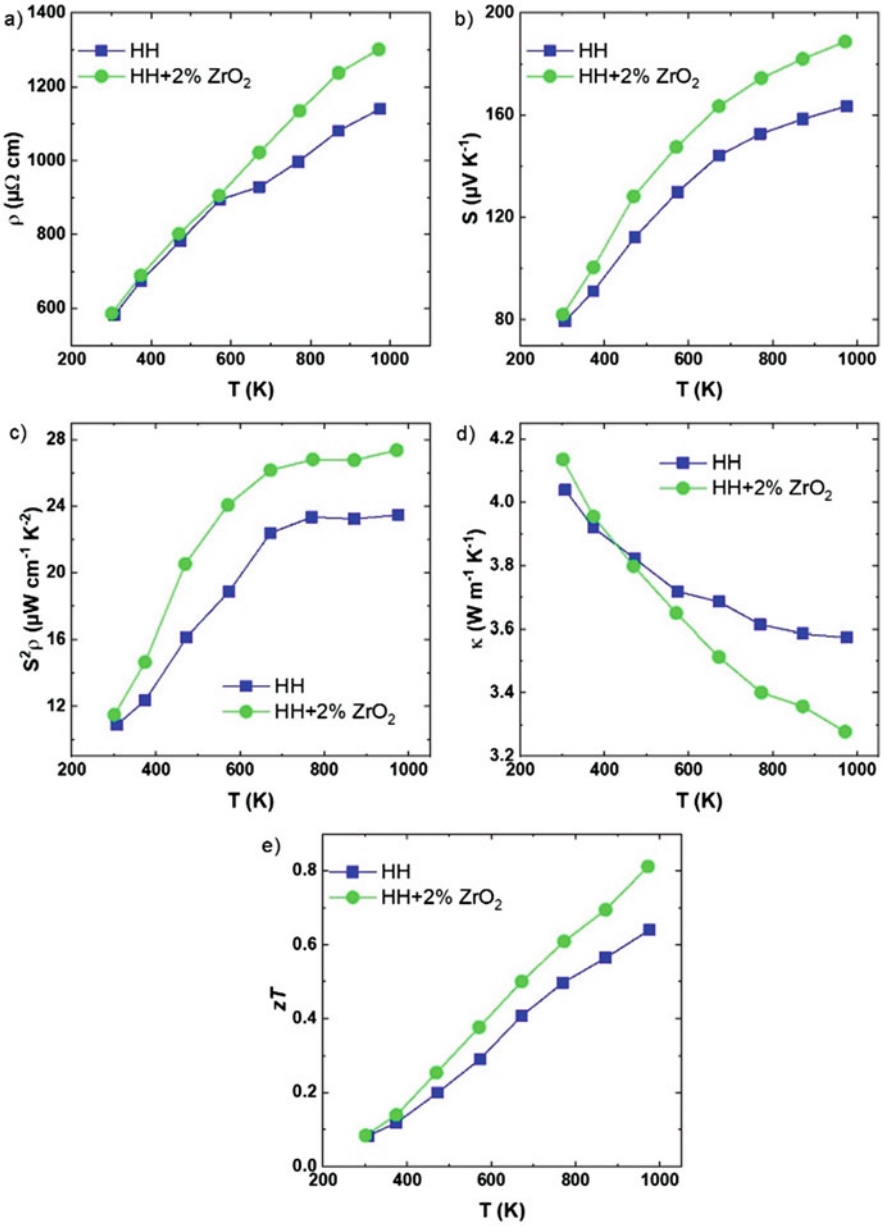

Fig. 10.6 Temperature-dependent (**a**) ρ, (**b**) S, (**c**) PF, (**d**) κ, and (**e**) ZT of p-type $Hf_{0.3}Zr_{0.7}CoSn_{0.3}Sb_{0.7}$ with and without 2 vol. % ZrO_2 additive of nanoparticles [31]

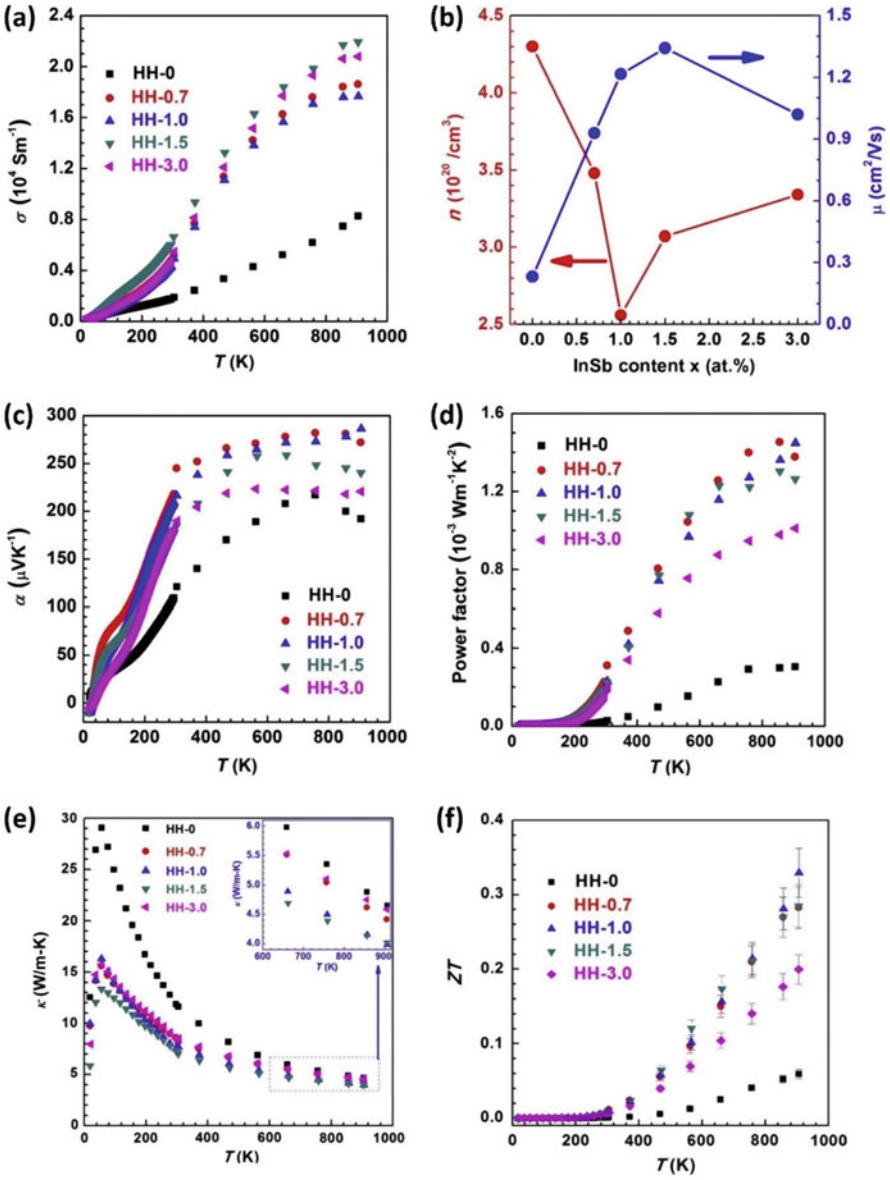

Fig. 10.7 (**a**) Temperature-dependent σ. (**b**) Dependences of concentration and mobility of charge carriers on InSb content. Temperature-dependent (**c**) S, (**d**) PF, (**e**) κ, and (**f**) ZT of $TiCo_{0.85}Fe_{0.15}Sb$ with different amount of InSb nanoinclusions [34]

Phase Separation

Another effective approach for reducing κ is phase separation. Rausch et al. studied systematically the effects of phase separation in TE performance of *M*CoSb-based HH compounds [38–40]. Typically, raw element materials were arc melted to form initial ingots. These ingots were annealed at 900 °C for 7 days and treated by ice water cooling. Figure 10.8a, b shows secondary electron image (SEM) with clearly visible multiple phases in the samples with nominal composition $Zr_{0.5}Hf_{0.5}CoSb_{0.8}Sn_{0.2}$ and $Ti_{0.5}Hf_{0.5}CoSb_{0.8}Sn_{0.2}$. Clearly, Hf − Ti diatomic system is more obvious in phase separation than Hf − Zr diatomic system due to similar atomic radii between Hf and Zr. This is further demonstrated in Table 10.1.

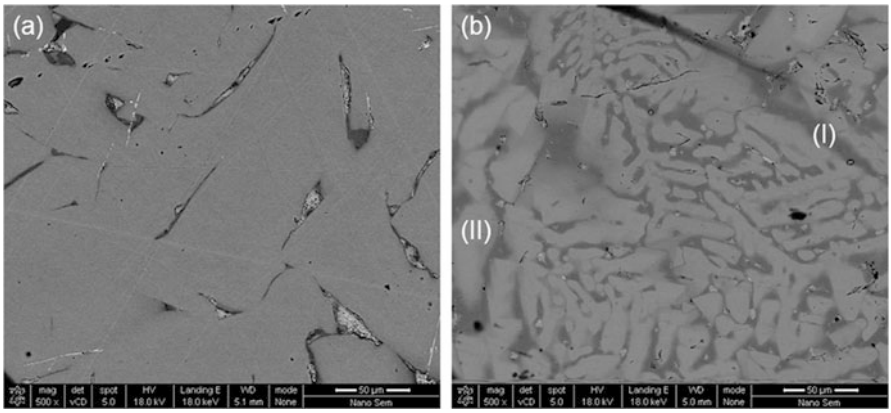

Fig. 10.8 SEM image of (**a**) $Zr_{0.5}Hf_{0.5}CoSb_{0.8}Sn_{0.2}$ and (**b**) $Ti_{0.5}Hf_{0.5}CoSb_{0.8}Sn_{0.2}$ [38]

Table 10.1 The nominal compositions; energy-dispersive X-ray spectroscopy (EDX) measured average compositions and separated phases of $MCoSb_{0.8}Sn_{0.2}$ [38]

M	EDX composition	Phases
Ti	$Ti_{0.97}Co_{0.99}Sb_{0.79}Sn_{0.25}$	$Ti_{1.01}Co_{0.97}Sb_{0.91}Sn_{0.01}$
		$Ti_{0.91}Co_{1.19}Sb_{0.23}Sn_{0.67}$
Zr	$Zr_{1.01}Co_{0.96}Sb_{0.77}Sn_{0.25}$ $Zr_{1.01}Co_{0.96}Sb_{0.15}Sn_{0.88}$	$Zr_{1.02}Co_{0.96}Sb_{0.87}Sn_{0.16}$
		$Zr_{1.01}Co_{0.96}Sb_{0.15}Sn_{0.88}$
Hf	$Hf_{1.07}Co_{0.93}Sb_{0.80}Sn_{0.20}$	$Hf_{1.11}Co_{0.92}Sb_{0.83}Sn_{0.14}$
		$Hf_{0.89}Co_{1.28}Sb_{0.07}Sn_{0.76}$
$Ti_{0.5}Zr_{0.5}$	$Ti_{0.49}Zr_{0.50}Co_{0.94}Sb_{0.89}Sn_{0.18}$	$Ti_{0.45}Zr_{0.56}Co_{0.96}Sb_{0.94}Sn_{0.09}$
		$Ti_{0.64}Zr_{0.38}Co_{0.98}Sb_{0.89}Sn_{0.13}$
$Zr_{0.5}Hf_{0.5}$	$Zr_{0.47}Hf_{0.56}Co_{0.94}Sb_{0.84}Sn_{0.19}$	$Zr_{0.47}Hf_{0.56}Co_{0.93}Sb_{0.88}Sn_{0.15}$
		$Zr_{0.52}Hf_{0.51}Co_{0.97}Sb_{0.72}Sn_{0.28}$
$Ti_{0.5}Hf_{0.5}$	$Ti_{0.52}Hf_{0.56}Co_{0.98}Sb_{0.65}Sn_{0.29}$	(I) $Ti_{0.65}Hf_{0.31}Co_{1.21}Sb_{0.23}Sn_{0.61}$[a]
		(II) $Ti_{0.38}Hf_{0.70}Co_{0.98}Sb_{0.84}Sn_{0.1}$[a]

[a]Roman numbers correspond to the areas in Fig. 10.8b

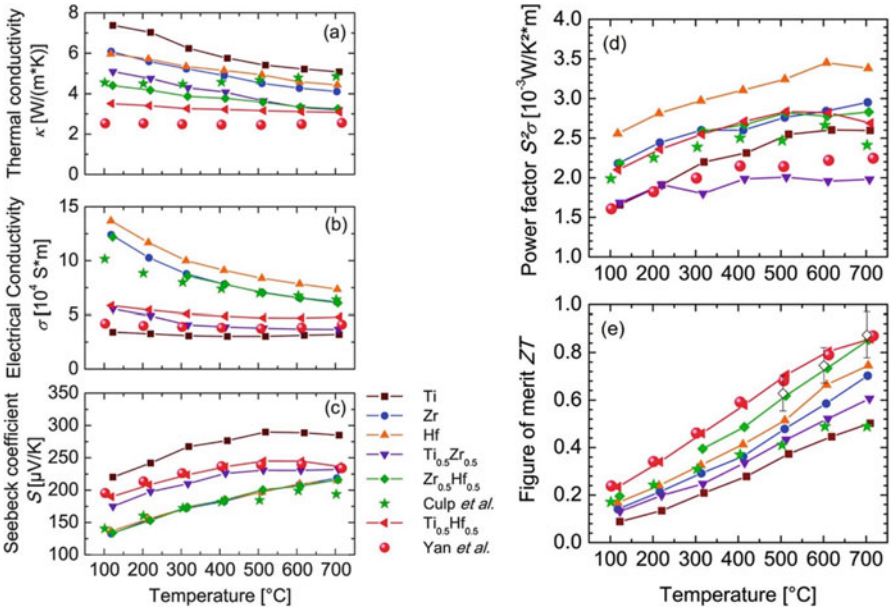

Fig. 10.9 Temperature-dependent (**a**) κ_L, (**b**) σ, (**c**) S, (**d**) PF, and (**e**) ZT of MCOSb$_{0.8}$Sn$_{0.2}$with phase separation. For comparison, TE properties of bulk ingots (star) and nanostructured (ball) $Hf_{0.5}Zr_{0.5}CoSb_{0.8}Sn_{0.2}$ are also plotted [38]

Figure 10.9 shows TE properties of phase-separated MCoSb$_{0.8}$Sn$_{0.2}$. For comparison, bulk (Culp et al. [41]) and nano-bulk (Yan et al. [2]) structured $Hf_{0.5}Zr_{0.5}CoSb_{0.8}Sn_{0.2}$ are plotted also in Fig. 10.9. $Hf_{0.5}Zr_{0.5}CoSb_{0.8}Sn_{0.2}$ with phase separation possesses much lower κ than that of the bulk ingot, as shown in Fig. 10.9a. On the other hand, both σ and S of $Hf_{0.5}Zr_{0.5}CoSb_{0.8}Sn_{0.2}$ with phase separation are similar to the bulk ingots, as shown in Fig. 10.9b, c. Accordingly, PF and ZT are plotted in Fig. 10.9d, e, respectively. Maximal ZT equals to approximately 0.9 at 700 °C for $Ti_{0.5}Hf_{0.5}$ and $Zr_{0.5}Hf_{0.5}$, which is comparable to the nano-bulk structured compound.

10.3 Enhancing Power Factor

10.3.1 Band Engineering

The thermoelectric effect in the solid is the result of electrical and thermal transport under electric field and temperature gradient. Electrical properties are determined mainly by the band structure and doping concentration of the materials. For HH compounds, the band structure could be considered as rigid and behavior of charge

carriers usually fits well to single parabolic band (SPB) model within reasonable doping levels. These features facilitate the manipulation and analysis of electronic properties of HH compounds.

One important strategy to enhance PF is band engineering. Schmitt et al. and Xie et al. analyzed the band structure of ZrNiSn using different approaches and revealed the existence of certain amount of Ni at 4*d* vacancy site (¾, ¾, ¾) [42–44]. The interstitial Ni yields an impurity band in the gap of ordered ZrNiSn, which is beneficial to *n*-type properties but undermines *p*-type performance of ZrNiSn. Importantly, this work reveals the sensitivity of band structures at atomic scale.

Subsequently, Fu et al. compared TE performances of *p*-type $Nb_{0.6}V_{0.4}FeSb$ and NbFeSb [7, 45]. The substitution of V at Nb site broadens of band edge and enhances of effective mass. The enhanced effective mass decreases in mobility of charge carriers and yields low PF. Therefore, higher TE performances were obtained by eliminating V. Peak PF ~ 47 $\mu W \times cm^{-1} \times K^{-2}$ at 900 K was reported in *p*-type NbFeSb with concentration of charge carriers of ~1.9×10^{21} cm^{-3}, while for $Nb_{0.6}V_{0.4}FeSb$, PF is equal to only ~30 $\mu W \times cm^{-1} \times K^{-2}$ at similar doping levels.

In another work by Zhu et al., the band structures of ZrCoBi, ZrCoSb, and TiCoSb were comparatively investigated [20]. As shown in Fig. 10.10a, the valence band maxima (VBM) locates at Γ point (marked by blue color), while the valence band at *L* point (marked by red color) show a negligible energy difference (ΔE) of ~0.001 eV lower than that of Γ point. Due to the negligible energy difference, all the valence bands that converge at *L* and Γ points will contribute jointly to the hole transport, therefore, in total yielding a high band degeneracy of 10 for *p*-type ZrCoBi (Fig. 10.10b). To highlight such a high band degeneracy in ZrCoBi, band structures for isostructural HHs ZrCoSb (Fig. 10.10c) and TiCoSb (Fig. 10.10e) were also calculated for comparison. In contrast, there is an appreciable energy difference of *L* and Γ points for ZrCoSb ($\Delta E \sim 0.13$ eV) and TiCoSb ($\Delta E \sim 0.11$ eV), which means only the valence bands at one of the points will contribute to the hole transport. To better illustrate the differences in band degeneracy among the three compounds, iso-energy surface at 0.1 eV below VBM is plotted (Fig. 10.10b, d, f). The band degeneracy equals to 8 for ZrCoSb and only 3 for TiCoSb, both of which are noticeably lower than that of ZrCoBi.

Due to the band convergence, higher PF is expected [46]. The electronic properties of doped ZrCoBi are shown in Fig. 10.11. Figure 10.11a, b shows σ and *S* of Sn-doped ZrCoBi. It is noteworthy that pristine ZrCoBi shows an intrinsic *n*-type transport characteristic, and Sn doping (Sn content as low as ~ 5 at. %) converts it successfully into fully *p*-type. The combined conductivity and *S* yield PF, as shown in Fig. 10.11c. For comparison, PF of ZrCoSb and TiCoSb with similar concentration of charge carriers are also plotted. Clearly, Sn-doped ZrCoBi shows noticeably higher PF than that of Sn-doped ZrCoSb and TiCoSb. Furthermore, band degeneracy-dependent PF at different temperatures is further plotted for the three compounds, as shown in Fig. 10.11d. PF increases monotonically with the band degeneracy at all of the temperatures. This unambiguously demonstrates that band degeneracy plays a pivotal role in PF. In other words, the high PF achieved in ZrCoBi-based compounds should be mainly ascribed to high band degeneracy for this compound as indicated by the theoretical calculations (Fig. 10.11b).

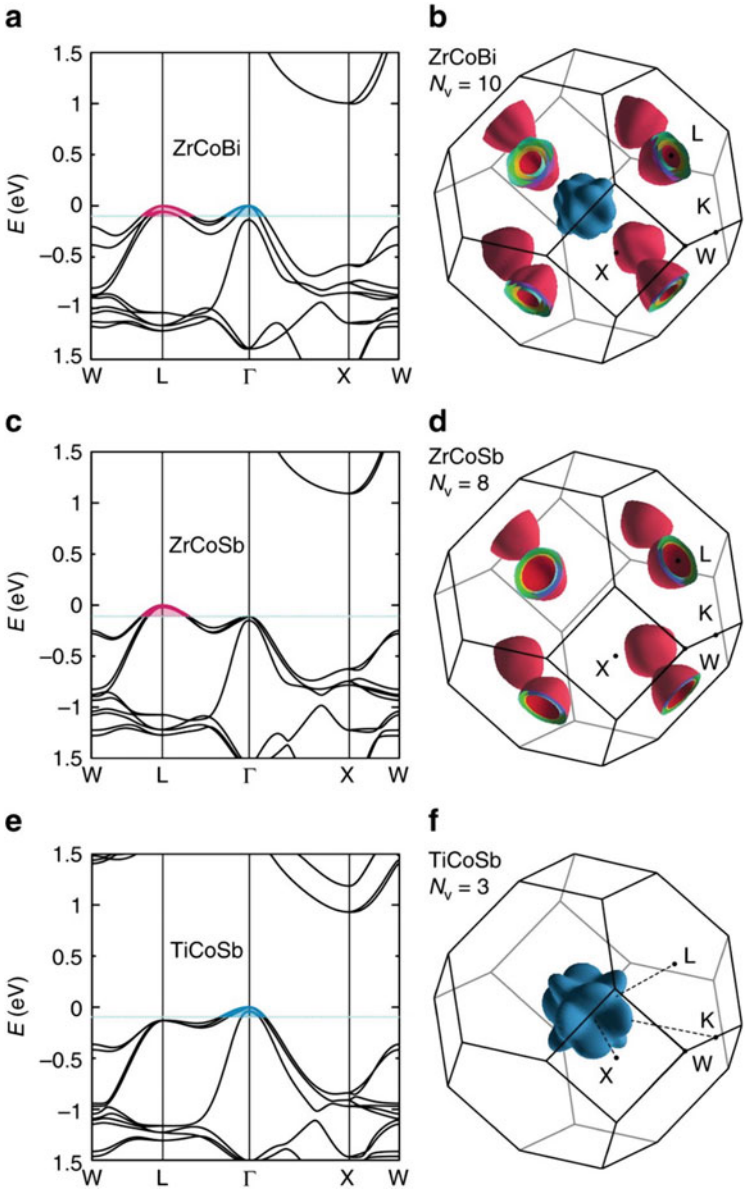

Fig. 10.10 First principle calculation of band structure. Calculated band structures of (**a**) ZrCoBi, (**c**) ZrCoSb, and (**e**) TiCoSb. The blue lines represent energy level of 0.1 eV below VBM. The corresponding iso-energy surfaces at 0.1 eV below VBM in Brillouin zone of (**b**) ZrCoBi, (**d**) ZrCoSb, and (**f**) TiCoSb [20]

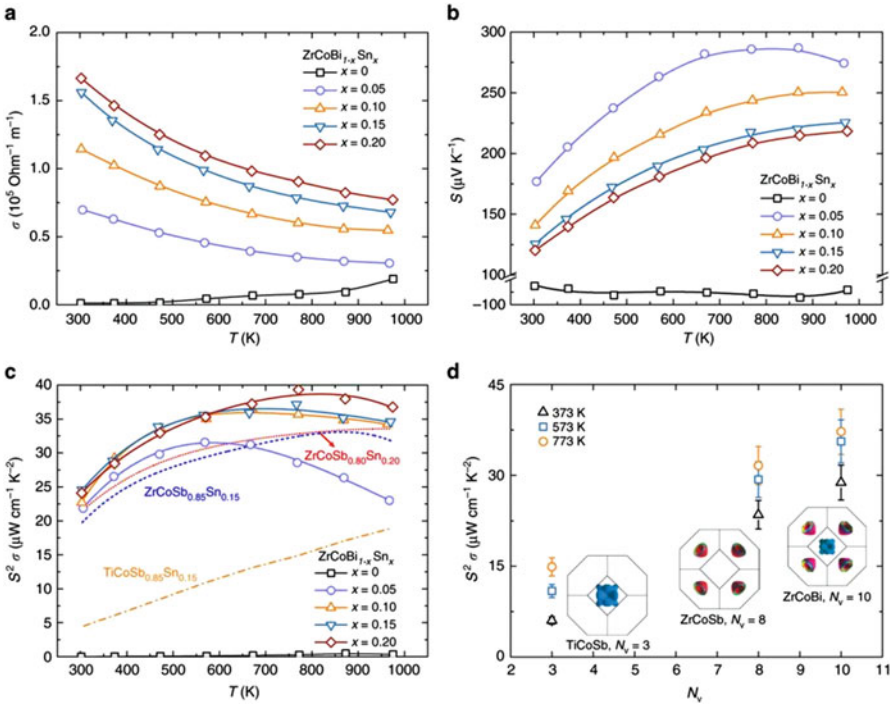

Fig. 10.11 Electrical properties of $ZrCoBi_{1-x}Sn_x$. Temperature-dependent (**a**) σ, (**b**) S, and (**c**) PF of $ZrCoBi_{1-x}Sn_x$ ($x = 0$, 0.05, 0.10, 0.15, and 0.20). (**d**) Band degeneracy-dependent PF for 15 at. % Sn-doped TiCoSb, ZrCoSb, and ZrCoBi at different temperatures with concentration of charge carriers of 1.62×10^{21}, 1.47×10^{21}, and 2.2×10^{21} cm^{-3}, respectively

10.3.2 Tuning the Scattering Mechanisms

Free charge carriers may interact with multiple scattering centers such as acoustic and optical phonons, ionized and neutral impurities, structural defects (dislocations, vacancies, et al.) and other obstacles. In most good TE materials, charge carriers scatter mostly by acoustic phonons and ionized impurities. For acoustic phonon scattering, the lattice vibrations are represented by longitudinal and transverse waves. When these waves are propagated along a crystal, an additional periodic potential is superimposed on the internal periodic potential. This alters the energy structure of the crystal, which is equivalent to an alternating potential energy of charge carriers, known as the deformation potential. On the other hand, an ionized impurity center in the lattice of a semiconductor produces long-range Coulomb field, which scatters charge carrier. The ionized impurity scattering is highly related to the amount of guest atoms and defects. Problems of mixed scattering have been considered with Boltzmann type electron gas in calculations of σ, Hall coefficient R_H, S,

and Nernst-Ettingshausen effect [47]. A simpler consideration involves power-law dependence of mobility of charge carriers with respect to temperature. For heavily doped semiconductor, mobility of charge carriers follows $\sim T^{-3/2}$ and $\sim T^{3/2}$ variation trends if the dominate scattering originates from acoustic phonons and ionized impurities, respectively. Tuning scatter mechanisms from ionized impurities to acoustic phonons was shown effective in improving TE performance in Mg_3Sb_2-based compounds [48]. Similar effects were also observed in HH compounds $Nb_{0.95}Ti_{0.05}FeSb$ with different sintering temperatures. By increasing sintering temperature, variation of σ with respect to temperature gradually approaches to $\sim T^{-3/2}$ law in the vicinity of room temperature (Fig. 10.12a) [16]. As a result, the value of PF at room temperature increases from ~50 $\mu W \times cm^{-1} \times K^{-2}$ to ~106 $\mu W \times cm^{-1} \times K^{-2}$, as shown in Fig. 10.12b. The obtained PF is not only the highest among HH compounds but also much higher than most TE materials. This work validates the effectiveness in improve TE performances by tuning scattering mechanisms of charge carriers.

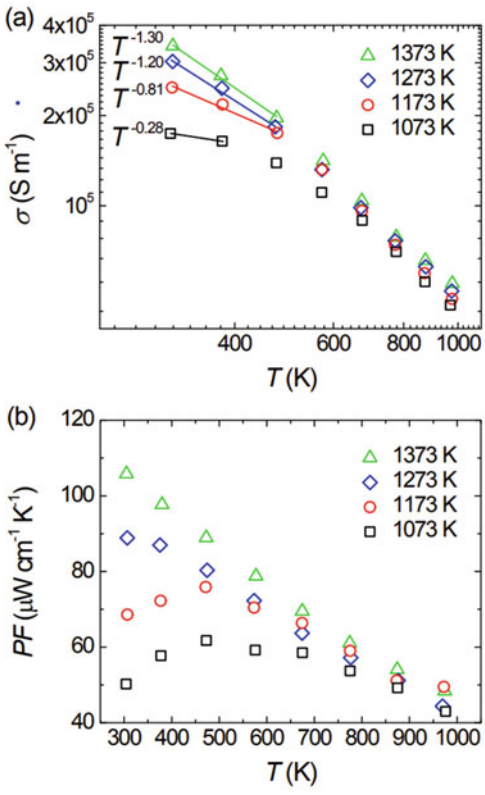

Fig. 10.12 Temperature dependences (**a**) σ and (**b**) PF of $Nb_{0.95}Ti_{0.05}FeSb$ sintered at temperatures 1073 K, 1173 K, 1273 K and 1373 K [16]

10.3.3 Energy Filter Effect

Based on Mott formula, Seebeck coefficient can be written as:

$$S = \frac{\pi^2}{3} \times \frac{k_B}{q} \times k_B T \left\{ \frac{d[\ln(\sigma(E))]}{dE} \right\}_{E=E_F} = \frac{\pi^2}{3} \times \frac{k_B}{q} \times k_B T \left\{ \frac{1}{n} \frac{dn(E)}{dE} + \frac{1}{\mu} \frac{d\mu(E)}{dE} \right\}_{E=E_F}, \quad (10.9)$$

where q, E_F, $n(E)$, and $\mu(E)$ are electron charge, Fermi energy, concentration, and mobility of charge carriers at energy E, respectively [49]. Enhancing both $\frac{dn(E)}{dE}$ and $\frac{d\mu(E)}{dE}$ will lead to high S, where the latter case can be realized through selective scattering of low-energy charge carriers near E_F, also named energy filtering effect. To enable scattering, potential barriers near E_F are necessary. In principle, any types of interfaces can produce potential barriers, but effective barriers require sophisticate designs. For example, single-phase boundaries, such as defective grain boundaries, may induce potential barriers. However, Bachmann et al. point out theoretically that double Schottky barriers due merely to the surface states are determined by chemical potential and concentrations of charge carriers as well [50]. When the matrix is heavily doped with concentration of charge carriers above 10^{20} cm^{-3}, potential barriers may become screened and ineffective. The paper suggests also other selective scattering centers, such as structural disorders at the grain boundaries, can still result in energy filtering.

Heterojunctions, where electronic band mismatch of different compositions takes place, can also create barriers together with the structural disorders. For instance, Chen et al. sintered 0, 3, 6, and 9 vol. % ZrO_2 nanoparticles with n-type $Zr_{0.5}Hf_{0.5}Ni_{0.8}Pd_{0.2}Sn_{0.99}Sb_{0.01}$ [29]. The resulting grain size of ZrO_2 is around 20 nm. The samples with 6 and 9 vol. % ZrO_2 both show increased in absolute value peak S of ~ −170 μV/K, compared to ~ −150 μV/K of ZrO_2 free sample. However, mobilities of charge carriers are reduced with increasing in vol. % of ZrO_2. Correspondingly, the sample with 9 vol. % ZrO_2 exhibits the highest resistivity and the lowest PF among all samples. The sample with 6 vol. % ZrO_2 shows ~15% enhanced PF compared with ZrO_2 free sample (~30 $\mu W \times cm^{-1} \times K^{-2}$ vs. ~26 $\mu W \times cm^{-1} \times K^{-2}$). In addition to physical mixing of two compounds to create heterojunctions, the interfaces can also be produced by in situ precipitation. For instance, Xie et al. produced (0, 1, 3, and 7 at. %) InSb nanoinclusions (10–300 nm) at the grain boundaries of $Ti_{0.5}Zr_{0.25}Hf_{0.25}Co_{0.95}Ni_{0.05}Sb$ via induction melting, pulverization, and spark plasma sintering [33]. Bulk InSb has higher mobility of charge carriers ~ 10^4 $cm^2/(V \times s)$ compared with HH matrix 1–10 $cm^2/(V \times s)$. However, in this work, mobilities of charge carriers reduced after introducing InSb, which is probably due to enhanced boundary scatterings. Increased S in the samples with InSb suggest

that the scattering is stronger toward low-energy electrons. In addition, these boundaries serve as dopants to improve σ. Among different samples, the one with 1 at. % InSb shows the highest S and σ with PF improved by nearly twofold at 570 K ($\sim$15 $\mu W \times cm^{-1} \times K^{-2}$) compared with that of HH matrix. Interestingly, Xie et al. observed also enhanced S in p-type HH with 0.7, 1.0, 1.5, and 3.0 at. % InSb nanoinclusions [34]. The sample preparation follows the same procedure as that of n-type work. However, electron mobility increases with InSb concentration and is higher than that of the sample without InSb. This trend is opposite to n-type HH case. In addition, the samples contain InSb all show higher S compared with InSb free sample. The authors again attribute it to the energy filtering effect at InSb-HH interfaces. Overall, the sample with 1.0 at. % InSb shows the highest peak $S \sim 285\ \mu V \times K^{-1}$ at 900 K. It also exhibits the highest PF = 15 $\mu W \times cm^{-1} \times K^{-2}$ at 900 K, i.e., ~360% improvement compared with InSb free sample.

Another type of heterojunction, coherent interfaces between in situ formed HH matrix and FH nanoinclusion (HH/FH), has been studied extensively, especially, by Poudeu's group [36, 37, 51–56]. The most interesting property of these interfaces is structural coherency, which leads to both energy filtering and preservation of charge mobilities, in contrast to reduced mobilities due to the incoherent boundaries introduced in previous paragraph. The effectiveness of such interfaces is reported in both n-type HH and p-type HH. In general, FH has composition of XY_2Z. The coherent HH/FH interfaces can be formed by adding excessive Y during the alloying of XYZ. The distinct crystal structures of FH (space group $Fm\bar{3}m$) and HH (space group $F\bar{4}3m$) lead to phase separation and formation of FH inclusions in HH matrix, while the similar atomic distributions of FH and HH result in coherent boundaries. Although bulk FH is metallic, at the dimension of 10 nm and below, quantum confinement can turn FH to semiconducting. Accordingly, the potential barriers near HH/FH vary significantly. In addition, Fermi level of HH matrix can be tuned by doping. Last, the distances between barriers should be greater than carrier momentum relaxation length and less than carrier energy relaxation length [57]. Therefore, size, number density, and distribution of FH, as well as, composition of HH matrix, all play important roles in energy filtering.

For example, in n-type HH $Zr_{0.25}Hf_{0.75}NiSn$ compound, extra Ni (2 at. % and 5 at. %, respectively) was added during solid-state reaction of elements in powder forms [37]. The mixture was held at $\sim 10^{-4}$ Torr and 1173 K for 2 days. TEM observation indicates formation of $Zr_{0.25}Hf_{0.75}Ni_2Sn$ nanoinclusions in both samples. In the sample containing 2 at. % extra Ni, nanoinclusions' sizes range from <1 to 3 nm and HH/FH interfaces are coherent. The room temperature S is 67% higher than that of pure HH matrix. The authors attribute the enhancement to energy filtering by HH/FH interfaces, as they observed a threefold decrease in room temperature concentration of charge carriers (from 5.6×10^{19} cm^{-3} for HH matrix to 1.9×10^{19} cm^{-3} for the sample with FH). Interestingly, the authors also observe 80% increase in mobility of charge carriers at 300 K. They propose that the higher mobility is due to weakened electron-electron scattering when concentration of charge carriers decreases.

In the sample with 5 at. % extra Ni, sizes of FH nanoinclusions increase to 1–20 nm, and lamellar structures with 2–8 nm thick and up to 30 nm long show up. As a result, the large metallic FH nanoinclusions serve as dopants, and the room temperature concentration of charge carriers nearly doubles that of HH matrix, despite the energy filtering at HH/FH interfaces. This again indicates the importance of size control of FH. Besides using $Zr_{0.25}Hf_{0.75}NiSn$ matrix, energy filtering by HH/FH is also effective with $Zr_{0.25}Hf_{0.75}Ni_{1+x}Sn_{0.975}Bi_{0.025}$ [37] and $Ti_{0.1}Zr_{0.9}Ni_{1+x}Sn$ [52] as the matrix, which is evidenced by decrease in concentration of charge carriers, higher mobility, and improved S after introducing FH nanoinclusions. However, if HH matrix is heavily doped by Sb in solid-state reaction produced $Zr_{0.25}Hf_{0.75}Ni_{1+x}Sn_{1-y}Sb_y$ ($y = 0.01,\ 0.025$) [55] and $Ti_{0.1}Zr_{0.9}Ni_{1+x}Sn_{0.975}Sb_{0.025}$ [53], energy filtering at HH/FH is greatly suppressed, especially when large (>20 nm) FH inclusions exist. This can be explained by large population of Sb and metallic FH-introduced extrinsic charge carriers, whose energy is high enough to cross the potential barrier. Furthermore, ball milling of the ingots obtained by solid-state reactions will significantly increase in the number of small FH nanoinclusions (<10 nm) and boost the effect of energy filtering, even when HH matrix is heavily doped $Ti_{0.4}Hf_{0.6}Ni_{1+x}Sn_{0.975}Sb_{0.025}$ [54].

The stability of FH inclusion on HH matrix has been studied by Chai, et al. on *n*-type $ZrNi_{1.1}Sn$ [56]. The materials were prepared by arc melting and solidified by optical floating zone method. As-prepared material contains $ZrNi_2Sn$ FH nanoprecipitates in plate (semi-coherent, average size of 330 nm long, 20 nm thick, and 100 nm wide) and disk (coherent, average size of $\sim$ 110 nm in diameter and $\sim$ 7 nm thick) morphologies. These nanoprecipitates orient preferentially along $\langle 001 \rangle$ directions of ZrNiSn HH matrix, and the interfaces are sharp under TEM [56, 58, 59]. Room temperature S of as-prepared sample is equal to $-208\ \mu V \times K^{-1}$, which is 20% higher than that of ZrNiSn ($-170\ \mu V \times K^{-1}$), presumably due to the energy filtering effect from the precipitates. In contrast, after the sample is measured up to 1073 K and cooled down, room temperature S drops to $-180\ \mu V \times K^{-1}$ and does not change much after another heating-cooling cycle. TEM shows that size of precipitates decreases to <20 nm after the cycles. However, smaller precipitates do not lead to stronger energy filtering as expected based on Poudeu's papers. The authors attribute the suppressed energy filtering to a reduced sharpness of HH/FH interfaces, stronger effect than size reduction, after the sample being heated to above the dissolution temperature of FH precipitates (1067 K).

In *p*-type HH, Poudeu's group firstly reports that HH/FH interfaces enable also energy filtering in $Ti_{0.5}Hf_{0.5}Co_{1+x}Sb_{0.9}Sn_{0.1}$ ($x = 0,\ 0.04,\ 0.05,\ 0.06,\ 0.07,\ 0.08$) [35]. The samples were prepared by solid-state reactions of elements in powder form at 10^{-4} Torr and 1173 K for 14 days. The powders were then sintered at 900 °C and 100 MPa. At $x = 0.05$, 5–60 nm spherical FH nanoinclusions are formed with coherent to semi-coherent interfaces with HH matrix. At room temperature, hole concentration in sample with $x = 0.05$ is equal to $\sim 2.8 \times 10^{20}\ cm^{-3}$, which is much lower than that of HH matrix ($\sim 8.0 \times 10^{20}\ cm^{-3}$). The authors exclude electron doping from metallic FH as the reason of reduced hole concentration, because excitations of intrinsic charge carriers are negligible at room temperature. In addition, room temperature hole mobility increases from ~0.9 to ~1.5 $cm^2/(V \times s)$.

The increase may be due to the following reasons: (1) suppressed scattering of charge carriers with decreased hole concentration, (2) weakened scattering by ionized impurities due to spatial separation of ionized impurities in HH matrix and holes in the valence band of FH inclusion, and (3) higher mobility of charge carriers with higher energy (passing through the energy barriers at HH/FH interfaces). At 300 K, as x increases from 0.05 to 0.08, σ increases from 62 S $\times$ cm^{-1} to 135 S $\times$ cm^{-1}, while S drops from 300 to 140 μV $\times$ K^{-1}. The origin of such changes isn't discussed in the paper. Nevertheless, even at $x = 0.08$, S of HH/FH composite sample is still 40% higher than that of HH matrix, indicating effective energy filtering at HH/FH boundaries. Besides this work, Chauhan et al. report also about energy filtering due to HH/FH interfaces in another p-type compound, $ZrCo_{1+x}Sb_{0.9}Sn_{0.1}$ (x = 0.01, 0.03, 0.05) [36].

Overall, energy filtering takes place at varied types of boundaries in HH. At that, incoherent interfaces degrade mobility of charge carriers and are less favorable than coherent ones. However, the existence of interface potential barriers and energy filtering effects is speculated through transport measurements on the whole samples. More work on quantifying magnitude of individual potential barrier and efficient controls of dimension, distribution, microstructure, and electronic structures of interfaces are challenging but highly desired.

10.4 Summary

In this chapter, we introduced TE properties of half-Heusler compounds. Promising ZT and PF have been found in material systems including *M*CoSb, *M*NiSn, NbFeSb, ZrCoBi, etc. Peak ZT values of 1–1.5 were reported in a variety of compounds. A record high output power density of ~22 W $\times$ cm^{-2} was also realized in NbFeSb-based compounds. Specifically, we summarize the strategies for improving thermoelectric performance. Band engineering, tuning scattering mechanisms of charge carriers, and energy filtering effects are the common strategies for PF enhancement; meanwhile nano-bulk structuring, alloying effects, and phase separations, etc. have been experimentally demonstrated effective to reduce κ_L. The success of these strategies suggests also the great potentials of half-Heusler compounds for power generation applications.

References

1. T. Graf, C. Felser, S.S.P. Parkin, Prog. Solid State Chem. **39**(1), 1–50 (2011)
2. X. Yan, G. Joshi, W. Liu, Y. Lan, H. Wang, S. Lee, J.W. Simonson, S.J. Poon, T.M. Tritt, G. Chen, Z.F. Ren, Nano Lett. **11**(2), 556–560 (2011)
3. X. Yan, W. Liu, H. Wang, S. Chen, J. Shiomi, K. Esfarjani, H. Wang, D. Wang, G. Chen, Z. Ren, Energy Environ. Sci. **5**(6), 7543 (2012)

4. X. Yan, W. Liu, S. Chen, H. Wang, Q. Zhang, G. Chen, Z. Ren, Adv. Energy Mater. **3**(9), 1195–1200 (2013)
5. G. Joshi, R. He, M. Engber, G. Samsonidze, T. Pantha, E. Dahal, K. Dahal, J. Yang, Y. Lan, B. Kozinsky, Z. Ren, Energy Environ. Sci. **7**(12), 4070–4076 (2014)
6. J. Yu, C. Fu, Y. Liu, K. Xia, U. Aydemir, T.C. Chasapis, G.J. Snyder, X. Zhao, T. Zhu, Adv. Energy Mater. **8**(1), 1701313 (2018)
7. C. Fu, T. Zhu, Y. Liu, H. Xie, X. Zhao, Energy Environ. Sci. **8**(1), 216–220 (2015)
8. S. Chen, K.C. Lukas, W. Liu, C.P. Opeil, G. Chen, Z. Ren, Adv. Energy Mater. **3**(9), 1210–1214 (2013)
9. G. Joshi, T. Dahal, S. Chen, H. Wang, J. Shiomi, G. Chen, Z. Ren, Nano Energy **2**(1), 82–87 (2013)
10. C. Yu, T.-J. Zhu, R.-Z. Shi, Y. Zhang, X.-B. Zhao, J. He, Acta Mater. **57**(9), 2757–2764 (2009)
11. H. Xie, H. Wang, Y. Pei, C. Fu, X. Liu, G.J. Snyder, X. Zhao, T. Zhu, Adv. Funct. Mater. **23** (41), 5123–5130 (2013)
12. G. Rogl, P. Sauerschnig, Z. Rykavets, V.V. Romaka, P. Heinrich, B. Hinterleitner, A. Grytsiv, E. Bauer, P. Rogl, Acta Mater. **131**, 336–348 (2017)
13. R. He, S. Gahlawat, C. Guo, S. Chen, T. Dahal, H. Zhang, W. Liu, Q. Zhang, E. Chere, K. White, Z. Ren, Phys. Status Solidi A **212**(10), 2191–2195 (2015)
14. G. Rogl, A. Grytsiv, M. Gürth, A. Tavassoli, C. Ebner, A. Wünschek, S. Puchegger, V. Soprunyuk, W. Schranz, E. Bauer, H. Müller, M. Zehetbauer, P. Rogl, Acta Mater. **107**, 178–195 (2016)
15. R. He, H.S. Kim, Y. Lan, D. Wang, S. Chen, Z. Ren, RSC Adv. **4**(110), 64711–64716 (2014)
16. R. He, D. Kraemer, J. Mao, L. Zeng, Q. Jie, Y. Lan, C. Li, J. Shuai, H.S. Kim, Y. Liu, D. Broido, C.-W. Chu, G. Chen, Z. Ren, Proc. Natl. Acad. Sci. **113**(48), 13576–13581 (2016)
17. C. Fu, S. Bai, Y. Liu, Y. Tang, L. Chen, X. Zhao, T. Zhu, Nat. Commun. **6**, 8144 (2015)
18. Y. Liu, C. Fu, K. Xia, J. Yu, X. Zhao, H. Pan, C. Felser, T. Zhu, Adv. Mater. **30**, e1800881 (2018)
19. R. He, H. Zhu, J. Sun, J. Mao, H. Reith, S. Chen, G. Schierning, K. Nielsch, Z. Ren, Mater. Today Phys. **1**, 24–30 (2017)
20. H. Zhu, R. He, J. Mao, Q. Zhu, C. Li, J. Sun, W. Ren, Y. Wang, Z. Liu, Z. Tang, Nat. Commun. **9**(1), 2497 (2018)
21. D.T. Morelli, G.A. Slack, High lattice thermal conductivity solids, in *High Thermal Conductivity Materials*, ed. by S. L. Shindé, J. S. Goela, (Springer, New York, NY, 2006)
22. J. Callaway, Phys. Rev. **113**(4), 1046–1051 (1959)
23. E.S. Toberer, A. Zevalkink, G.J. Snyder, J. Mater. Chem. **21**(40), 15843–15852 (2011)
24. M. Zhou, L. Chen, C. Feng, D. Wang, J.-F. Li, J. Appl. Phys. **101**(11), 113714 (2007)
25. X.Y. Huang, Z. Xu, L.D. Chen, X.F. Tang, Key Eng. Mater. **249**, 79–82 (2003)
26. X.Y. Huang, Z. Xu, L.D. Chen, Solid State Commun. **130**(3–4), 181–185 (2004)
27. R. Yaqub, P. Sahoo, J.P.A. Makongo, N. Takas, P.F.P. Poudeu, K.L. Stokes, Sci. Adv. Mater. **3** (4), 633–638 (2011)
28. D.K. Misra, J.P.A. Makongo, P. Sahoo, M.R. Shabetai, P. Paudel, K.L. Stokes, P.F.P. Poudeu, Sci. Adv. Mater. **3**(4), 607–614 (2011)
29. L.D. Chen, X.Y. Huang, M. Zhou, X. Shi, W.B. Zhang, J. Appl. Phys. **99**(6), 064305 (2006)
30. X.Y. Huang, L.D. Chen, X. Shi, M. Zhou, Z. Xu, Key Eng. Mater. **280–283**, 385–388 (2007)
31. S.J. Poon, D. Wu, S. Zhu, W. Xie, T.M. Tritt, P. Thomas, R. Venkatasubramanian, J. Mater. Res. **26**(22), 2795–2802 (2011)
32. C.-C. Hsu, Y.-N. Liu, H.-K. Ma, J. Alloys Compd. **597**, 217–222 (2014)
33. W.J. Xie, J. He, S. Zhu, X.L. Su, S.Y. Wang, T. Holgate, J.W. Graff, V. Ponnambalam, S.J. Poon, X.F. Tang, Acta Mater. **58**(14), 4705–4713 (2010)
34. W.J. Xie, Y.G. Yan, S. Zhu, M. Zhou, S. Populoh, K. Gałązka, S.J. Poon, A. Weidenkaff, J. He, X.F. Tang, T.M. Tritt, Acta Mater. **61**(6), 2087–2094 (2013)
35. P. Sahoo, Y. Liu, J.P.A. Makongo, X.-L. Su, S.J. Kim, N. Takas, H. Chi, C. Uher, X. Pan, P.F.P. Poudeu, Nanoscale **5**(19), 9419 (2013)

36. N.S. Chauhan, A. Bhardwaj, T.D. Senguttuvan, R.P. Pant, R.C. Mallik, D.K. Misra, J. Mater. Chem. C **4**(24), 5766–5778 (2016)
37. J.P.A. Makongo, D.K. Misra, X. Zhou, A. Pant, M.R. Shabetai, X. Su, C. Uher, K.L. Stokes, P.F.P. Poudeu, J. Am. Chem. Soc. **133**(46), 18843–18852 (2011)
38. E. Rausch, B. Balke, S. Ouardi, C. Felser, Phys. Chem. Chem. Phys. **16**(46), 25258–25262 (2014)
39. E. Rausch, B. Balke, T. Deschauer, S. Ouardi, C. Felser, APL Mater. **3**(4), 041516 (2015)
40. E. Rausch, B. Balke, S. Ouardi, C. Felser, Energ. Technol. **3**(12), 1217–1224 (2015)
41. S.R. Culp, J.W. Simonson, S.J. Poon, V. Ponnambalam, J. Edwards, T.M. Tritt, Appl. Phys. Lett. **93**(2), 022105 (2008)
42. J. Schmitt, Z.M. Gibbs, G.J. Snyder, C. Felser, Mater. Horiz. **2**(1), 68–75 (2015)
43. H.-H. Xie, J.-L. Mi, L.-P. Hu, N. Lock, M. Chirstensen, C.-G. Fu, B.B. Iversen, X.-B. Zhao, T.-J. Zhu, Cryst. Eng. Comm. **14**(13), 4467 (2012)
44. H. Xie, H. Wang, C. Fu, Y. Liu, G.J. Snyder, X. Zhao, T. Zhu, Sci. Rep. **4**(1), 6888 (2014)
45. C. Fu, T. Zhu, Y. Pei, H. Xie, H. Wang, G.J. Snyder, Y. Liu, Y. Liu, X. Zhao, Adv. Energy Mater. **4**(18), 1400600 (2014)
46. Y. Pei, X. Shi, A. LaLonde, H. Wang, L. Chen, G.J. Snyder, Nature **473**(7345), 66–69 (2011)
47. J.P. Heremans, C.M. Thrush, D.T. Morelli, Phys. Rev. B **70**(11), 115334 (2004)
48. J. Shuai, J. Mao, S. Song, Q. Zhu, J. Sun, Y. Wang, R. He, J. Zhou, G. Chen, D.J. Singh, Z. Ren, Energy Environ. Sci. **10**(3), 799–807 (2017)
49. M. Cutler, N.F. Mott, Phys. Rev. **181**(3), 1336–1340 (1969)
50. M. Bachmann, M. Czerner, C. Heiliger, Phys. Rev. B **86**(11), 245115 (2012)
51. J.P.A. Makongo, D.K. Misra, J.R. Salvador, N.J. Takas, G. Wang, M.R. Shabetai, A. Pant, P. Paudel, C. Uher, K.L. Stokes, P.F.P. Poudeu, J. Solid State Chem. **184**(11), 2948–2960 (2011)
52. Y. Liu, P. Sahoo, J.P.A. Makongo, X. Zhou, S.-J. Kim, H. Chi, C. Uher, X. Pan, P.F.P. Poudeu, J. Am. Chem. Soc. **135**(20), 7486–7495 (2013)
53. Y. Liu, A. Page, P. Sahoo, H. Chi, C. Uher, P.F.P. Poudeu, Dalton Trans. **43**(21), 8094–8101 (2014)
54. P. Sahoo, Y. Liu, P.F.P. Poudeu, J. Mater. Chem. A **2**(24), 9298–9305 (2014)
55. Y. Liu, J.P.A. Makongo, A. Page, P. Sahoo, C. Uher, K. Stokes, P.F.P. Poudeu, J. Solid State Chem. **234**, 72–86 (2016)
56. Y.W. Chai, T. Oniki, Y. Kimura, Acta Mater. **85**, 290–300 (2015)
57. Y. Nishio, T. Hirano, Jpn. J. Appl. Phys. **36**(Part 1, 1A), 170–174 (1997)
58. Y.W. Chai, Y. Kimura, Acta Mater. **61**(18), 6684–6697 (2013)
59. Y. Wang Chai, Y. Kimura, Appl. Phys. Lett. **100**(3), 033114 (2012)